PCCP

ROYAL SOCIETY OF CHEMISTRY

PAPER

View Article Online
View Journal

Cite this: DOI: 10.1039/d6cp00933f

High-level *ab initio* characterization of the multichannel $Cl(^2P_{3/2})$ + C_2H_5I reaction

Csaba Rudner, Balázs Gruber and Gábor Czakó *

The potential energy surface (PES) of the $Cl(^2P_{3/2})$ + C_2H_5I reaction is described by highly-accurate electronic structure computations, covering both hydrogen- and iodine-abstraction pathways and several substitution routes proceeding through either Walden inversion or front-side attack, including both atom- (H, I) and group-exchange (CH_2I, CH_3) mechanisms. Geometries and harmonic vibrational frequencies of all stationary points are determined at the MP2/aug-cc-pVDZ and CCSD(T)-F12b/aug-cc-pVDZ levels of theory, and single-point energies are further refined at the most accurate geometries using the coupled-cluster method with aug-cc-pVTZ and aug-cc-pVQZ basis sets. To target chemical accuracy, five additional energy corrections – accounting for core correlation, scalar relativistic, spin–orbit, and post-CCSD(T) effects – are incorporated into the CCSD(T)-F12b/aug-cc-pVQZ single-point energies. The resulting benchmark data allow for the detailed mapping of the reaction pathways, including the identification of transition states and pre- and post-reaction minima, which guide the system from the reactants toward the various product channels on the PES. Rate coefficients are determined using transition-state theory, including the Wigner tunneling correction, and compared to literature theoretical values.

Received 13th March 2026,
Accepted 28th May 2026

DOI: 10.1039/d6cp00933f

rsc.li/pccp

I. Introduction

Metabolic activity in marine macroalgae and phytoplankton releases a diverse set of iodine-bearing organic compounds, including small iodinated volatiles such as ethyl-iodide (C_2H_5I), into coastal and open-ocean atmospheres, and such iodinated species influence ozone loss indirectly by generating reactive iodine through two distinct pathways.[1–6] One route involves photolytic dissociation, with near-ultraviolet absorption leading to the release of iodine atoms with high quantum yields.[7,8] A second pathway operates through oxidative degradation initiated by several atmospheric oxidants, among them chlorine atoms.[9–13]

Available studies on the reaction of Cl + C_2H_5I concentrate mainly on the kinetic perspective and offer little information on the underlying energetics or stationary structures. Studies addressing the kinetics and product distribution of the Cl + C_2H_5I reaction identify two principal pathways – association of Cl with C_2H_5I to form a molecular adduct ($C_2H_5I\cdots Cl$) and H-abstraction that produces HCl and $C_2H_4I^\bullet$ – and show that adduct formation becomes effectively stabilized at low temperatures, where the $C_2H_5I\cdots Cl$ complex does not readily dissociate, whereas at higher temperatures rapid predissociation suppresses complex stabilization and renders H-abstraction the dominant reaction pathway.[12–16] Experimental determinations of the $C_2H_5I\cdots Cl$ adduct formation enthalpy were reported from UV absorption measurements, complemented by IR detection of HCl formed in the H-abstraction channel.[8] On the theoretical side, reaction enthalpies for the formation of the $C_2H_5I\cdots Cl$ adduct were computed by Orlando and co-workers[8] and by Enami *et al.*[15] using density-functional methods, and Wada and co-workers[17] also evaluated the adduct formation enthalpy using MP2/aug-cc-pVTZ structures together with CCSD single-point refinements. Beyond the characterization of the adduct, theoretical work on reaction pathways remains limited, with one study in particular reporting stationary points that connect reactants to products. Jia and co-workers identified transition structures for two H-abstraction pathways, corresponding to abstraction from the α and β carbon sites, as well as for an I-substitution channel, with geometries optimized at the MP2 level using 6-311++G(d,p) basis functions for carbon and hydrogen as well as aug-cc-pVTZ and aug-cc-pVTZ-PP basis sets for chlorine and iodine, respectively, and relative energies refined through CCSD(T) single-point calculations employing the same 6-311++G(d,p) basis for carbon and hydrogen together with aug-cc-pVTZ for chlorine and aug-cc-pVTZ-PP for iodine.[18] Further insight into one of the key products of the H-abstraction pathway, the iodoethyl radical ($C_2H_4I^\bullet$), was provided by a series of experimental and theoretical studies. Time-resolved X-ray diffraction measurements, together with earlier structural and computational investigations, showed that the radical stabilizes in a bridged geometry rather than in the classical anti form.[19–22]

MTA-SZTE Lendület "Momentum" Computational Reaction Dynamics Research Group, Interdisciplinary Excellence Centre and Department of Physical Chemistry and Materials Science, Institute of Chemistry, University of Szeged, Rerrich Béla tér 1, Szeged H-6720, Hungary. E-mail: gczako@chem.u-szeged.hu

Given the limited information available on the energetics and stationary structures associated with the Cl + C_2H_5I reaction, the aim of the present study is to identify all relevant stationary points and thereby providing an accurate and high-level description of the reaction energetics, based on benchmark-quality geometries and relative energies computed with the gold-standard coupled-cluster method and an appropriate set of correlation-consistent basis functions, supplemented by additional contributions required for chemical accuracy. The reaction landscape is mapped in far greater detail than in previous studies, incorporating an extensive set of abstraction pathways – including H-abstraction from both the α and β carbon sites and iodine abstraction – as well as a broad range of substitution channels comprising iodine substitution, H-substitution at the α and β positions, and group-exchange processes involving CH_3 and CH_2I transfer, with all substitution pathways investigated along both Walden-inversion and front-side attack mechanisms. The resulting energetic and structural data offer a detailed and internally consistent representation of the potential energy surface (PES) and provide a firm foundation for theoretical kinetic modelling as well as future PES developments that enable advanced dynamical studies through trajectory simulations.

II. Computational details

Geometry optimizations and harmonic vibrational frequency calculations for all stationary points are first performed at the MP2/aug-cc-pVDZ[23,24] level of theory and subsequently refined at the CCSD(T)-F12b/aug-cc-pVDZ level.[25] Single-point energy computations are then carried out at the CCSD(T)-F12b/aug-cc-pVTZ[26] and CCSD(T)-F12b/aug-cc-pVQZ[25,26] levels to minimize basis-set convergence errors. For the iodine atom, a relativistic effective core potential (ECP)[27,28] is applied for all stationary points to replace the 28 inner-core electrons ($1s^22s^22p^63s^23p^63d^{10}$), together with the corresponding pseudopotential basis sets aug-cc-pV*n*Z-PP (*n* = D, T, and Q),[27,28] utilizing the revised ECP and basis set parameters of ref. 28.

Using the geometries optimized at the CCSD(T)-F12b/aug-cc-pVDZ level, additional energy corrections ((a)–(e)) are evaluated to further enhance the accuracy of the computed energies.

(a) Core-correlation correction (Δ_{core}): the contribution of the inner-shell electrons is accounted for by subtracting the frozen-core (FC) results from the all-electron (AE) values, both obtained with the aug-cc-pwCVTZ basis set:[29]

$$\Delta_{core} = \Delta E(\text{AE-CCSD(T)/aug-cc-pwCVTZ}) - \Delta E(\text{FC-CCSD(T)/aug-cc-pwCVTZ}) \quad (1)$$

Note that in the case of Cl and I AE means the correlation of the $2s^22p^63s^23p^5$ and $4s^24p^64d^{10}5s^25p^5$ electrons, respectively, in accordance with the development of the aug-cc-pwCVTZ and aug-cc-pwCVTZ-PP (used for I) basis sets.

(b) Scalar relativistic correction (Δ_{rel}): scalar relativistic effects (beyond what are described by the ECP used for I) are estimated using the second-order Douglas–Kroll (DK)[30] approach with the aug-cc-pwCVTZ-DK basis set:[31,32]

$$\Delta_{rel} = \Delta E(\text{DK-AE-CCSD(T)/aug-cc-pwCVTZ-DK}) - \Delta E(\text{AE-CCSD(T)/aug-cc-pwCVTZ}) \quad (2)$$

((c) and (d)) Post-CCSD(T) correlation corrections (δ[T] and δ[(Q)]): higher-order correlation effects beyond the perturbative triples (CCSD(T))[33] are evaluated at the CCSDT[34] and CCSDT(Q)[35] levels using the cc-pVDZ basis set:

$$\delta[\text{T}] = \Delta E(\text{CCSDT/cc-pVDZ}) - \Delta E(\text{CCSD(T)/cc-pVDZ}) \quad (3)$$

and

$$\delta[(\text{Q})] = \Delta E(\text{CCSDT(Q)/cc-pVDZ}) - \Delta E(\text{CCSDT/cc-pVDZ}) \quad (4)$$

(e) Spin–orbit correction (Δ_{SO}): since the system contains halogen atoms, spin–orbit (SO) coupling effects are explicitly considered to account for their energy-lowering contribution. The SO corrections are evaluated using the multireference configuration interaction method (MRCI)[36] with Davidson correction (+Q)[37] for the diagonal elements of the SO matrix, employing the Breit–Pauli operator[38] with the aug-cc-pVDZ basis set. In the MRCI computations 3 doublet electronic states are included and an active space consisting of 27 valence electrons distributed among 14 spatial orbitals is employed, while the 16 core orbitals are doubly occupied and are all closed and frozen. The SO contribution is obtained as the energy difference between the relativistic spin–orbit coupled (SO_1) and nonrelativistic (non-SO_1) ground states, both computed at the MRCI+Q level of theory:

$$\Delta_{SO} = SO_1(\text{MRCI+Q/aug-cc-pVDZ}) - \text{non-}SO_1(\text{MRCI+Q/aug-cc-pVDZ}) \quad (5)$$

Due to the fact that the above SO computation technique is not highly accurate for heavy elements like iodine, in the case of the product channels resulting in I atom, we utilize the experimental SO shift for the products obtained from the measured SO splitting of the I atom (ε = 21.74 kcal mol^{-1}) as SO_1 − non-SO_1 = $-\varepsilon/3$ = −7.25 kcal mol^{-1}.[39]

For each stationary point, the benchmark classical relative energy ($\Delta E_{Classical}$) is determined by adding all high-level corrections ((a)–(e)) to the corresponding CCSD(T)-F12b/aug-cc-pVQZ single-point value obtained at the CCSD(T)-F12b/aug-cc-pVDZ geometry:

$$\Delta E_{Classical} = \Delta E(\text{CCSD(T)-F12b/aug-cc-pVQZ}) + \delta[\text{T}] + \delta[(\text{Q})] + \Delta_{core} + \Delta_{rel} + \Delta_{SO} \quad (6)$$

The benchmark adiabatic energy ($\Delta E_{Adiabatic}$) is calculated by combining the benchmark classical energy with the zero-point vibrational contribution (ΔZPE) obtained from CCSD(T)-F12b/aug-cc-pVDZ frequency computations, or from MP2/aug-cc-pVDZ data when the former are unavailable:

$$\Delta E_{Adiabatic} = \Delta E_{Classical} + \Delta\text{ZPE} \quad (7)$$

All computations are performed using the MOLPRO 2015.1 program package,[40] except for the spin–orbit coupling corrections, which are determined with MOLPRO 2023.2.[41] The post-

(T) energy corrections are obtained with the MRCC program.[42] The coupled-cluster computations utilize the unrestricted formalism with ROHF reference, except eqn (3) and (4), where UHF orbitals are employed. In the CCSD(T)-F12b/aug-cc-pV*n*Z (n = D, T, Q) computations, the auxiliary basis sets are generated automatically in MOLPRO 2015: aug-cc-pV*n*Z/MP2FIT and cc-pV*n*Z/JKFIT (including JKFIT2) are utilized, while for iodine the corresponding aug-cc-pV*n*Z-PP basis is used. The complementary auxiliary basis (CABS) is constructed internally by the program using suitable alternative RI basis sets.

We also perform a kinetic study using standard transition-state theory (TST) to gain a clearer picture of which product channels are actually dominant. The thermal rate coefficients are determined as follows:

$$k(T) = \left(\frac{k_B T}{h}\right)\left(\frac{Q_{TS}}{Q_{Cl} Q_{C_2H_5I}}\right) e^{-\Delta E_a / RT} \quad (8)$$

where k_B is the Boltzmann constant, T is the temperature, h is the Planck constant, ΔE_a is the adiabatic barrier height, R is the gas constant, and Q_{TS}, Q_{Cl}, and $Q_{C_2H_5I}$ denote the partition functions of TS, Cl, and C_2H_5I, respectively. The molecular partition functions are represented as the product of translational (Q_{trans}), rotational (Q_{rot}), vibrational (Q_{vib}), and electronic (Q_{elec}) contributions. They are calculated using standard formulas, where the rigid rotor and harmonic oscillator approximations are used for the rotational and vibrational terms, respectively. The effect of tunneling is taken into account by the Wigner correction factor, which multiplicatively modifies the results by

$$\kappa(T) = 1 + \frac{1}{24}\left(\frac{h|\nu_{TS}|}{k_B T}\right) \quad (9)$$

where ν_{TS} is the imaginary frequency of the TS.

III. Results and discussion

One-dimensional potential energy curves are obtained to characterize the entrance channel of the Cl + C_2H_5I reaction. Nine distinct orientations are explored using the MP2 and CCSD(T)-F12b methods in combination with the aug-cc-pVDZ basis set, as shown in Fig. 1. Among the investigated orientations, only two orientations exhibit pronounced potential wells deeper than 1.5 kcal mol^{-1}, suggesting a considerable influence on the entrance-channel dynamics. In one favorable orientation, the Cl atom approaches the C_2H_5I molecule perpendicularly to the C–C bond from the iodine side, generating a minimum of approximately 7 kcal mol^{-1} at the MP2 level and nearly 11 kcal mol^{-1} at the coupled-cluster level. The corresponding C–Cl distance is close

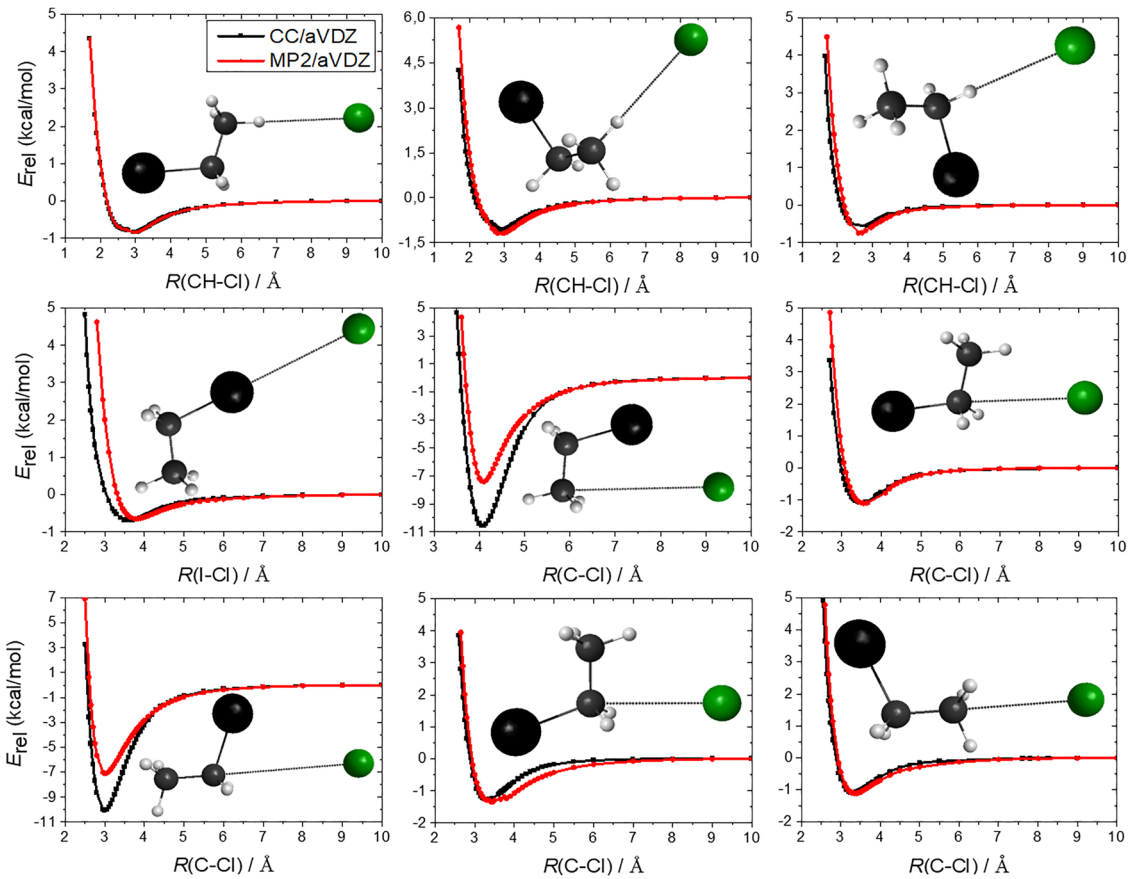

Fig. 1 One-dimensional potential energy curves for the entrance channel obtained along nine different orientations at the MP2/aug-cc-pVDZ (red) and CCSD(T)-F12b/aug-cc-pVDZ (black) levels of theory. The C_2H_5I molecule is kept frozen at its equilibrium geometry, while the intermolecular distance (dotted bond) is systematically varied.

to 4 Å. In another energetically preferred geometry, the Cl atom proceeds along the C–C bond axis toward the carbon atom bonded to iodine, yielding a similar minimum of around 7 kcal mol^{-1} at the MP2 level and about 10 kcal mol^{-1} at the CCSD(T)-F12b level, located near a 3 Å C–Cl distance in both cases. The positions of the potential minima obtained from the MP2 and coupled-cluster computations generally coincide, except for a single orientation in which the Cl atom approaches the iodine atom of C_2H_5I parallel to the I–C bond. Furthermore, MP2 and coupled-cluster methods provide nearly identical well depths in orientations where the minima are shallow, whereas in the two most favorable approaches, the coupled-cluster method yields potential wells that are typically deeper by almost 4 kcal mol^{-1} compared to MP2.

Two abstraction and four substitution pathways are investigated as potential reaction channels in this study using the obtained benchmark $\Delta E_{\text{Classical}}$ and $\Delta E_{\text{Adiabatic}}$ energies. Fig. 2 illustrates the schematic potential energy surface for the abstraction processes, encompassing both H- and I-abstraction pathways. The I-abstraction route is traced by red dashed lines, the H-abstraction channels are marked by blue dashed lines, and the relative energies with respect to the reactants are indicated as black values for benchmark classical results and red values for adiabatic energies including the zero-point energy corrections, alongside the most accurate optimized geometries. One-dimensional scans reveal two configurations associated with pronounced potential wells, and one of them, corresponding to the reactant-side minimum of the iodine-abstraction route (IABS preMIN complex), is successfully characterized through geometry optimization and confirmed as a true minimum on the potential energy surface by harmonic frequency analysis, with benchmark classical(adiabatic) relative energy of −12.85(−12.27) kcal mol^{-1}. Proceeding along this pathway, two distinct transition states are located beyond IABS preMIN, reflecting alternative orientations of the Cl atom during the approach. The first transition state (IABS TS1) corresponds to an in-line geometry where the Cl atom approaches over the C–C bond axis, whereas the second one (IABS TS2) features a more external attack directed toward the iodine atom from the side. The lower barrier is associated with IABS TS2, with a classical(adiabatic) relative energy of 11.47(10.11) kcal mol^{-1}, while IABS TS1 lies significantly higher, at 20.60(19.88) kcal mol^{-1} relative to the reactants. In the product-side region of the I-abstraction channel, two separate minima are found: IABS postMIN1 and IABS postMIN2. The latter has a classical(adiabatic) relative energy of 9.54(6.49) kcal mol^{-1}, only marginally above that of IABS postMIN1 by 0.44(0.35) kcal mol^{-1}. Upon separation of the fragments, the system attains the final products of the I-abstraction channel, ICl and the ethyl radical (C_2H_5), whose energy exceeds that of the reactants by 11.32(8.01) kcal mol^{-1} classically(adiabatically), confirming the endothermic character of the process. In addition, the reaction enthalpy values associated with the reactant-side minimum of the reaction channel (the IABS preMIN complex), which have been reported experimentally, are in good agreement with our results. In these studies, Orlando, Enami, Wada, and co-workers[8,15,17] derived experimental values using thermodynamic analyses of both the second and third law of motion. Our value shown above (−12.27 kcal mol^{-1}) is in best agreement with the experimental result of the third law of motion, which is −12.67 ± 1 kcal mol^{-1}.

While the iodine-abstraction channel involves the removal of the halogen atom, the reaction can also proceed *via* H abstraction, where the Cl atom removes a hydrogen atom from the C_2H_5I molecule. The H-abstraction process can occur at three distinct sites. The first possibility involves abstraction of the hydrogen attached to the carbon directly bonded to iodine. In addition, two alternative orientations are considered for abstraction from the

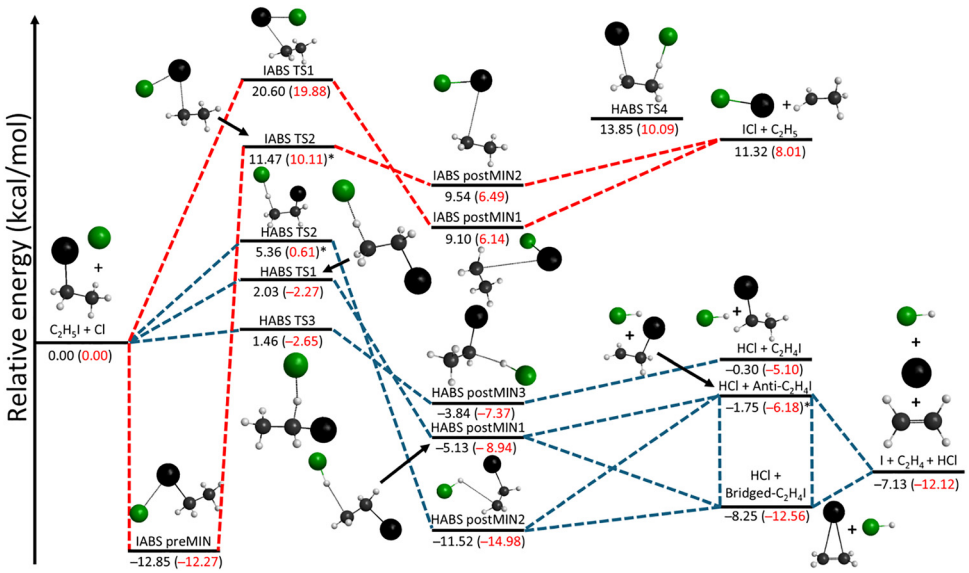

Fig. 2 Schematic potential energy surface for the abstraction pathways of the Cl($^2P_{3/2}$) + C_2H_5I reaction, showing the most accurate optimized geometries and the benchmark classical (black) and adiabatic (red) relative energies with respect to the reactants. The red dashed line represents the I-abstraction pathways, while the blue dashed lines indicate the H-abstraction pathways. * denotes energies at MP2/aug-cc-pVDZ geometries.

methyl group: the Cl atom can either remove one of the two equivalent hydrogens located on the same side as the iodine substituent or abstract the hydrogen positioned *trans* to the iodine atom. For each of these three orientations, a corresponding transition state is identified. The pathway in which the Cl atom abstracts the hydrogen attached to the carbon bonded to iodine (HABS TS3) exhibits the lowest barrier, with classical(adiabatic) relative energy of 1.46(−2.65) kcal mol^{-1}. The abstraction from the methyl group on the same side as the iodine substituent (HABS TS1) proceeds through a slightly higher barrier of 2.03(−2.27) kcal mol^{-1}, whereas the *trans*-oriented abstraction (HABS TS2) features the highest barrier, with classical(adiabatic) relative energy of 5.36(0.61) kcal mol^{-1}. Notably, when zero-point energy corrections are taken into account, two of the three possible H-abstraction channels proceed without an energy barrier. Furthermore, for each of the three H-abstraction orientations, a corresponding post-reaction minimum is identified in the product-side region. The energetic ordering of these minima differs from that of the transition states. The lowest-energy structure (HABS postMIN2) corresponds to the pathway in which the Cl atom abstracts one of the two equivalent hydrogens on the same side as the iodine substituent, with classical(adiabatic) relative energy of −11.52(−14.98) kcal mol^{-1}. The next in energy (HABS postMIN1) is associated with the channel where the Cl atom abstracts the hydrogen positioned *trans* to the iodine atom, featuring classical(adiabatic) relative energy of −5.13(−8.94) kcal mol^{-1}. The highest-energy post-reaction minimum (HABS postMIN3) is found for the abstraction from the carbon directly bonded to iodine, with corresponding classical(adiabatic) relative energy of −3.84(−7.37) kcal mol^{-1}. Depending on the carbon site from which the hydrogen atom is abstracted, the three H-abstraction pathways lead to two distinct product types, CH_3CHI and CH_2CH_2I, both formed together with an HCl molecule. When the abstraction occurs at the methyl group, the resulting CH_2CH_2I species exists in two different conformations. One corresponds to a geometry where the iodine atom is positioned above the C–C bond (Bridged), while the other adopts an arrangement in which the iodine atom points outward (Anti). Among the three possible product channels, the Bridged-CH_2CH_2I + HCl combination represents the lowest-energy product state, with classical(adiabatic) relative energy of −8.25(−12.56) kcal mol^{-1}. The Anti-CH_2CH_2I + HCl channel lies higher in energy, at −1.75(−6.18) kcal mol^{-1}, whereas the CH_3CHI + HCl pathway corresponds to the highest product energy, though it remains exothermic, with classical(adiabatic) relative energy of −0.30(−5.10) kcal mol^{-1}. The dissociation of the CH_2CH_2I molecule may occur, leading to a three-fragment product channel consisting of C_2H_4, atomic iodine, and HCl, with classical(adiabatic) relative energy of −7.13(−12.12) kcal mol^{-1} with respect to the reactants.

Fig. 3 displays the four substitution pathways of the Cl + C_2H_5I reaction, each represented by a distinct color – magenta

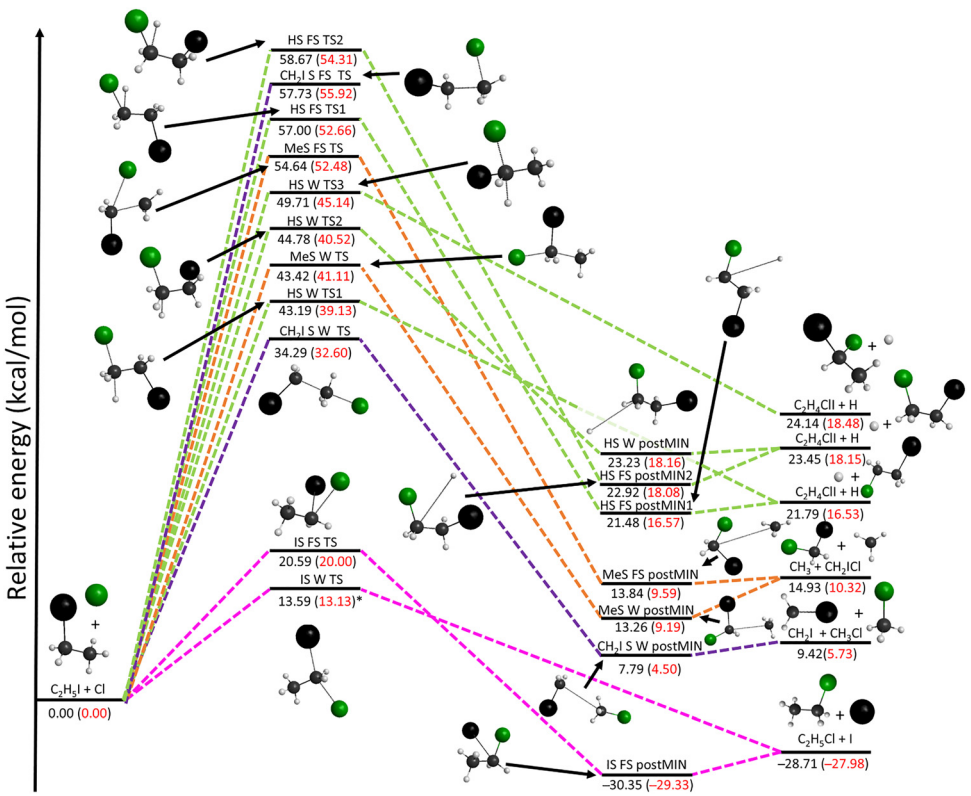

Fig. 3 Schematic potential energy surface for the substitution pathways of the Cl($^2P_{3/2}$) + C_2H_5I reaction, showing the most accurate geometries and the benchmark classical (black) and adiabatic (red) relative energies with respect to the reactants. The magenta dashed line represents the I-substitution pathway, the purple dashed line corresponds to the CH_2I-substitution pathway, the orange dashed line indicates the CH_3-substitution pathways, and the green dashed lines represent the H-substitution pathways. * denotes energies at MP2/aug-cc-pVDZ geometry.

for I-substitution, purple for CH_2I-substitution, green for H-substitution, and orange for CH_3-substitution – together with the most accurate optimized geometries of the stationary points located on each pathway. The I-substitution pathway emerges as the only thermodynamically favorable substitution process, producing CH_3CH_2Cl + I with 28.71(27.98) kcal mol^{-1} below that of the reactants classically(adiabatically), which renders it not only the most stable substitution channel but also the most exothermic product pathway among all investigated reactions. In addition to its pronounced thermodynamic preference, this pathway proceeds through the lowest energy barriers among the substitution mechanisms, with the transition state corresponding to the Walden inversion (IS W TS) appearing at 13.59(13.13) kcal mol^{-1} relative to the reactants, while the front-side attack (IS FS TS) involves a higher barrier located at 20.59(20.00) kcal mol^{-1}. The front-side route further features a post-reaction minimum (IS FS postMIN) in the exit channel, representing the global minimum of the entire potential energy surface, with classical(adiabatic) relative energy of −30.35(−29.33) kcal mol^{-1}. The CH_2I-substitution pathway emerges as the deepest among the endothermic substitution channels, following the I-substitution products in the overall energy order. Its products (CH_2I + CH_3Cl) lie 9.42(5.73) kcal mol^{-1} above the reactants classically(adiabatically). Two transition states are identified along this pathway: the Walden inversion (CH_2I S W TS) at 34.29(32.60) kcal mol^{-1} and the front-side attack (CH_2I S FS TS) at 57.73(55.92) kcal mol^{-1} relative to the reactants. Moreover, a post-reaction complex (CH_2I S W postMIN) is identified along the Walden-inversion pathway, exhibiting classical(adiabatic) relative energy of 7.79(4.50) kcal mol^{-1}. The CH_3-substitution pathway is slightly more endothermic than the CH_2I-substitution channel, with the products located 14.93(10.32) kcal mol^{-1} above the reactants classically(adiabatically). The reaction proceeds through two barriers that fall between those of the CH_2I-substitution route. The transition state of the Walden inversion (CH_3 S W TS) lies at 43.42(41.11) kcal mol^{-1} relative to the reactants, whereas the front-side attack (CH_3 S FS TS) requires 54.64(52.48) kcal mol^{-1}. Post-reaction complexes are identified for both mechanisms in the exit channel: the Walden-type process yields CH_3 S W postMIN at 13.26(9.19) kcal mol^{-1}, and the front-side pathway forms CH_3 S FS postMIN, which lies marginally higher in energy at 13.84(9.59) kcal mol^{-1} classically(adiabatically), consistent with the energetic order of the transition states. Taking both substitution and abstraction channels into account, the H-substitution pathways represent the most endothermic reactions, producing three distinct C_2H_4ClI-type products accompanied by an H atom. Among them, the trans-CH_2ClCH_2I + H channel represents the lowest-lying configuration, located 21.79(16.53) kcal mol^{-1} above the reactants classically(adiabatically). A slightly higher-energy pathway leads to the *cis* isomer (*cis*-CH_2ClCH_2I), in which the iodine and chlorine atoms are bonded to different carbon centers yet remain on the same molecular side, with relative energy of 23.45(18.15) kcal mol^{-1} classically(adiabatically). The route forming a product with both halogens attached to the same carbon atom ($CClHICH_3$) is the most endothermic, with energy exceeding that of the *cis* channel by 0.69(0.33) kcal mol^{-1}. The observed energetic sequence can be attributed to steric effects, as the large halogen substituents generate increasing repulsion when positioned in close proximity. Along the route leading to the trans-CH_2ClCH_2I + H products, two transition states (HS W TS1 and HS FS TS1) and one post-reaction minimum (HS FS postMIN1) are identified. The Walden-type transition state appears at 43.19(39.13) kcal mol^{-1} relative to the reactants, while the front-side attack involves a substantially higher barrier located at 57.00(52.66) kcal mol^{-1} classically(adiabatically). The minimum after the corresponding reaction shows a relative classical(adiabatic) energy of 21.48(16.57) kcal mol^{-1} for HS FS postMIN1. The *cis*-CH_2ClCH_2I + H pathway displays a slightly different energetic landscape. Two transition states (HS W TS2 and HS FS TS2) and two post-reaction complexes (HS W postMIN and HS FS postMIN2) are identified along this route as well. The Walden inversion occurs at 44.78(40.52) kcal mol^{-1}, whereas the front-side mechanism proceeds through a considerably higher barrier at 58.67(54.31) kcal mol^{-1}. For the *cis* configuration, the corresponding post-reaction minima do not preserve the same energetic order as the transition states, with classical(adiabatic) values of HS W postMIN and HS FS postMIN2 lying 23.23(18.16) and 22.92(18.08) kcal mol^{-1}, respectively. The most endothermic H-substitution pathway, leading to the $CClHICH_3$ + H products, features a single transition state (HS W TS3) corresponding to a Walden-type mechanism, with relative classical(adiabatic) energy of 49.71(45.14) kcal mol^{-1}.

Table 1 summarizes the relative energies of all identified stationary points, showing the values corresponding to the geometries optimized at the MP2/aug-cc-pVDZ and CCSD(T)-F12b/aug-cc-pVDZ levels of theory, along with the auxiliary and zero-point energy corrections computed at the most accurate optimized geometries, together with the resulting final classical and adiabatic relative energies. Notable discrepancies are observed between the MP2/aug-cc-pVDZ and CCSD(T)-F12b/aug-cc-pVDZ energies for several stationary points, with the largest deviation found for CH_2I S FS TS, where the difference between the two theoretical levels slightly exceeds 8 kcal mol^{-1}, reaching 8.32 kcal mol^{-1}. Comparison of the coupled-cluster energies obtained with the aug-cc-pVDZ, aug-cc-pVTZ, and aug-cc-pVQZ basis sets reveals that the differences are generally within 1 kcal mol^{-1}, and the transition from triple- to quadruple-zeta quality introduces even smaller changes, often below 0.1 kcal mol^{-1}, indicating excellent basis-set convergence of the explicitly-correlated method. Examination of the magnitudes of the five correction terms (δ[T], δ[(Q)], Δ_{core}, Δ_{rel}, and Δ_{SO}) clearly demonstrates that inclusion of these effects is indispensable for attaining subchemical accuracy in the relative energies of the characterized geometries, as the corresponding contributions often reach several tenths of a kcal mol^{-1} and, for certain stationary points, may even exceed 1 kcal mol^{-1}. Fig. 4 illustrates the relative contributions of the five correction terms, with each component represented by a distinct color. Among the auxiliary corrections, the spin–orbit effect clearly stands out as the most significant contribution, which is expected given the presence of two relatively heavy halogen atoms in the system, since both chlorine and iodine induce substantial changes in the total

Table 1 Energies and auxiliary energy components (kcal mol^{-1}) of the stationary points of the Cl($^2P_{3/2}$) + C_2H_5I reaction, relative to the reactants, including transition states, pre- and post-reaction minima, and products, computed at different theoretical levels

	MP2	CCSD(T)-F12b										
Stationary point	DZ[a]	DZ[b]	TZ[c]	QZ[d]	δ[T][e]	δ[Q][f]	Δ_{core}[g]	Δ_{rel}[h]	Δ_{SO}[i]	$\Delta E_{Classical}$[j]	Δ_{ZPE}[k]	$\Delta E_{Adiabatic}$[l]
CH_2I S FS TS	65.86	57.54	57.79	57.77	−0.82	−0.43	0.30	0.01	0.90	57.73	−1.81	55.92
CH_2I S W postMIN	13.16	6.47	6.99	6.85	−0.24	−0.04	0.19	0.20	0.83	7.79	−3.29	4.50
CH2I S W TS	39.44	34.01	33.91	33.86	−0.52	−0.34	0.34	0.05	0.90	34.29	−1.69	32.60
HABS TS1	2.53	1.04	1.52	1.46	−0.14	−0.17	−0.10	0.08	0.90	2.03	−4.30	−2.27
HABS TS2	5.69	—	—	—	−0.13	−0.16	−0.16	0.11	0.91	5.36	−4.75	0.61
HABS TS3	1.95	0.32	0.96	0.96	−0.13	−0.18	−0.17	0.09	0.89	1.46	−4.11	−2.65
HABS TS4	16.75	15.94	15.70	15.30	−0.46	−0.64	0.40	0.14	−0.89	13.85	−3.76	10.09
HABS postMIN1	−2.22	−5.75	−4.85	−4.93	−0.33	−0.14	0.04	0.26	−0.03	−5.13	−3.81	−8.94
HABS postMIN2	−3.09	−10.37	−9.86	−10.13	−0.15	−0.15	0.45	0.30	−1.83	−11.52	−3.46	−14.98
HABS postMIN3	−2.00	−5.51	−4.48	−4.49	−0.20	−0.08	−0.12	0.24	0.80	−3.84	−3.52	−7.37
HS FS TS1	60.96	56.04	56.81	56.78	−0.42	−0.36	0.08	0.01	0.91	57.00	−4.35	52.66
HS FS TS2	63.64	57.76	58.49	58.46	−0.37	−0.35	−0.01	0.03	0.91	58.67	−4.36	54.31
HS W TS1	44.52	42.40	44.39	44.33	−0.24	−0.29	0.00	0.08	0.91	43.19	−4.26	39.13
HS W TS2	45.70	43.80	42.90	42.85	−0.32	−0.36	0.03	0.09	0.91	44.78	−4.06	40.52
HS W TS3	51.10	48.70	49.40	49.33	−0.28	−0.39	0.02	0.11	0.91	49.71	−4.56	45.14
HS FS postMIN1	17.04	19.10	20.65	20.59	0.09	−0.17	−0.15	0.20	0.92	21.48	−4.90	16.57
HS FS postMIN2	19.06	20.67	22.18	22.09	0.08	−0.17	−0.21	0.21	0.92	22.92	−4.84	18.08
HS W postMIN	17.08	20.97	22.46	22.37	0.08	−0.17	−0.18	0.21	0.92	23.23	−5.07	18.16
I ABS TS1	26.80	23.39	22.93	22.61	−1.09	−0.64	0.60	0.09	−0.98	20.60	−0.72	19.88
I ABS TS2	22.26	—	11.29	10.95	−1.10	−0.43	1.07	0.14	0.84	11.47	−1.36	10.11
I ABS postMIN1	15.75	8.37	8.02	7.47	−0.17	−0.04	0.79	0.12	0.93	9.54	−2.96	6.49
I ABS postMIN2	16.55	8.88	8.47	7.89	−0.16	−0.04	0.80	0.12	0.93	9.10	−3.05	6.14
I ABS preMIN	−11.12	−13.70	−13.83	−14.02	0.10	0.11	−0.07	0.12	0.91	−12.85	0.58	−12.27
IS FS TS	26.80	23.39	22.93	22.61	−1.10	−0.64	0.60	0.09	−0.97	20.59	−0.59	20.00
IS W TS	13.59	—	—	—	—	—	—	—	—	13.59	−0.46	13.13
IS FS postMIN	−26.50	−27.61	−27.43	−27.74	−0.01	−0.02	0.73	0.30	−3.61	−30.35	1.02	−29.33
Me S FS TS	62.12	54.24	54.61	54.65	−0.79	−0.43	0.29	0.01	0.91	54.64	−2.16	52.48
Me S W TS	48.02	43.03	43.21	43.13	−0.52	−0.38	0.26	0.03	0.90	43.42	−2.31	41.11
Me S FS postMIN	15.98	12.06	12.98	12.82	−0.06	−0.07	0.04	0.18	0.93	13.84	−4.25	9.59
Me S W postMIN	15.20	11.50	12.37	12.23	−0.06	−0.07	0.05	0.18	0.93	13.26	−4.07	9.19
C_2H_4 + I +HCl	0.04	−1.61	−1.78	−2.15	−0.08	−0.04	1.16	0.30	−6.32	−7.13	−4.99	−12.12
CH_2I + CH_3Cl	15.35	8.05	8.54	8.33	−0.23	−0.02	0.32	0.18	0.84	9.42	−3.69	5.73
CH_3CHI +HCl	2.94	−1.73	−1.05	−1.16	−0.19	−0.04	0.03	0.22	0.84	−0.30	−4.80	−5.10
Bridged-C_2H_4I + HCl	—	−6.59	−6.33	−6.69	−0.18	−0.14	0.67	0.30	−2.21	−8.25	−4.31	−12.56
Anti-C_2H_4I + HCl	1.17	—	−1.93	−2.06	−0.24	−0.08	0.10	0.26	0.26	−1.75	−4.43	−6.20
trans-CH_2ClCH_2I + H	17.31	19.46	20.94	20.87	0.08	−0.17	−0.13	0.21	0.93	21.79	−5.26	16.53
C_2H_4ClI + H	19.11	21.72	23.39	23.32	0.13	−0.20	−0.23	0.19	0.93	24.14	−5.66	18.48
cis-CH_2ClCH_2I + H	26.44	21.17	22.66	22.57	0.09	−0.17	−0.18	0.21	0.93	23.45	−5.30	18.15
C_2H_5 + ICl	18.32	10.40	9.81	9.17	−0.16	−0.02	0.99	0.41	0.93	11.32	−3.31	8.01
C_2H_5Cl + I	−22.64	−23.65	−23.62	−23.89	0.02	0.02	1.14	0.32	−6.32	−28.71	0.73	−27.98
CH_2ClI + CH_3	17.25	13.16	13.93	13.86	−0.11	−0.09	0.16	0.18	0.93	14.93	−4.61	10.32

[a] MP2/aug-cc-pVDZ relative energies based on MP2/aug-cc-pVDZ geometries. [b] CCSD(T)-F12b/aug-cc-pVDZ relative energies based on CCSD(T)-F12b/aug-cc-pVDZ geometries. [c] CCSD(T)-F12b/aug-cc-pVTZ relative energies based on the most accurate geometries. [d] CCSD(T)-F12b/aug-cc-pVQZ relative energies based on the most accurate geometries. [e] CCSDT − CCSD(T) energies computed with the cc-pVDZ basis set at the most accurate geometries. [f] CCSDT(Q) − CCSDT energies computed with the cc-pVDZ basis set at the most accurate geometries. [g] Core-correlation correction obtained as the difference of all-electron and frozen-core CCSD(T)/aug-cc-pwCVTZ relative energies at the most accurate geometries. [h] Scalar relativistic correction obtained as the difference of DK-AE-CCSD(T)/aug-cc-pwCVTZ-DK and non-relativistic AE-CCSD(T)/aug-cc-pwCVTZ relative energies. [i] Spin-orbit correction obtained as the energy difference between SO and non-SO ground-state MRCI+Q/aug-cc-pVDZ calculations at the most accurate geometries. [j] Benchmark classical relative energy obtained as CCSD(T)-F12b/aug-cc-pVQZ + δ[T] + δ[(Q)] + Δ_{core} + Δ_{rel} + Δ_{SO}. [k] ΔZPE computed at the most accurate level where geometry optimization succeeded. [l] Benchmark adiabatic relative energy obtained as $\Delta E_{Classical}$ + Δ_{ZPE}.

energy through relativistic coupling. For most stationary points, the magnitude of the Δ_{SO} correction falls in the range of 0.8–1.0 kcal mol^{-1}. It is also noteworthy that for five stationary points, the Δ_{SO} value exceeds 1.83 kcal mol^{-1} in absolute terms, and for two of these, corresponding to the C_2H_4 + I + HCl and C_2H_5Cl + I products, the Δ_{SO} contribution reaches 6.32 kcal mol^{-1}. The pronounced increase in the magnitude of the correction originates from the replacement of the lighter chlorine atom in the reactant by the heavier iodine atom in the product channel, where the liberated open-shell iodine exhibits far stronger spin–orbit coupling than either the bonded iodine or the atomic chlorine in the reactants, resulting in substantially larger Δ_{SO} corrections. The remaining four corrections contribute modestly to the total energy, with absolute values typically below 1 kcal mol^{-1}, although a few deviations are observed, as the δ[T] term yields corrections of −1.09 and −1.10 kcal mol^{-1} for the IABS TS1 and IABS TS2 stationary points, while the Δ_{core} contribution exceeds 1 kcal mol^{-1} for IABS TS2, C_2H_4 + I + HCl, and C_2H_5Cl + I, corresponding to 1.07, 1.16, and 1.14 kcal mol^{-1}, respectively. The benchmark classical energies ($\Delta E_{Classical}$) are derived from the CCSD(T)-F12b/aug-cc-pVQZ single-point values (except for HABS TS2 and IS W TS, where the MP2/aug-cc-pVDZ results are used due to convergence

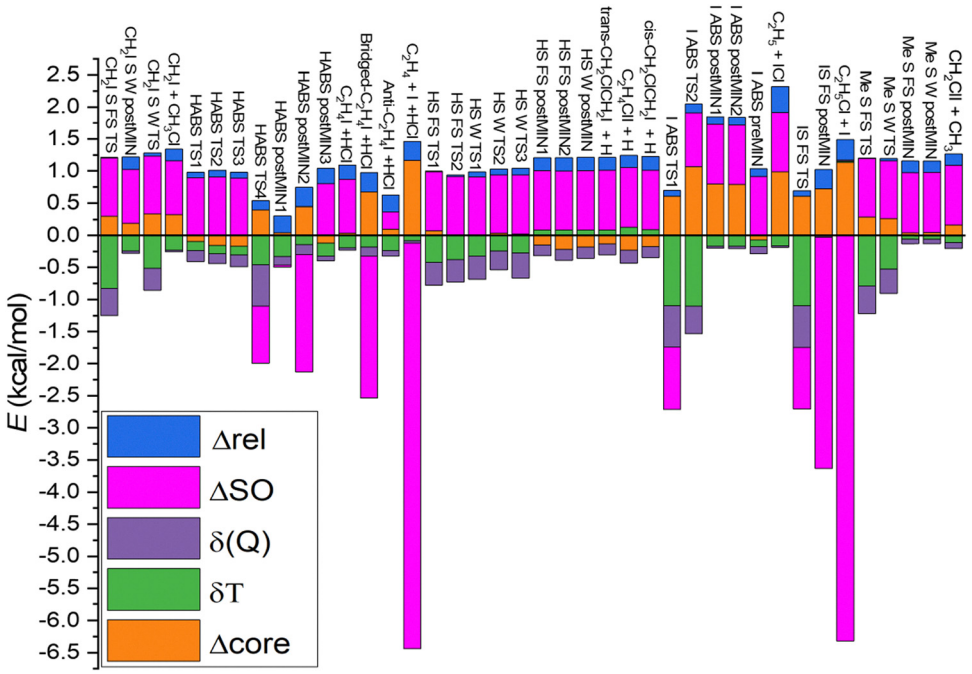

Fig. 4 Bar chart illustrating the contributions of the correction terms for all stationary points of the $Cl(^2P_{3/2})$ + C_2H_5I reaction, where the relativistic correction (Δ_{rel}) is shown in blue, the spin–orbit correction (Δ_{SO}) in magenta, the δ[(Q)] correction in purple, the δ[T] correction in green, and the core correlation correction (Δ_{core}) in orange.

issues) by adding the five correction terms. Incorporation of the zero-point energy corrections to the classical energies produces the benchmark adiabatic energies ($\Delta E_{Adiabatic}$), allowing direct comparison with reaction enthalpies derived from the Active Thermochemical Tables (ATcT)[43] formation enthalpies according to Hess's law and yielding reaction enthalpies of -12.49 ± 0.12 kcal mol^{-1} for C_2H_4 + I + HCl (where our result is -12.12 kcal mol^{-1}), 5.28 ± 0.13 kcal mol^{-1} for C_2H_5 + ICl (where our result is 8.01 kcal mol^{-1}), and -28.22 ± 0.13 kcal mol^{-1} for C_2H_5Cl + I (where our result is -27.98 kcal mol^{-1}), showing good agreement within 0.4 kcal mol^{-1} for the C_2H_4 + I + HCl and C_2H_5Cl + I product channels. Only in the case of the C_2H_5 + ICl product channel is there a larger difference between the results, where the ATcT may be problematic, as our research group also found a substantial deviation between the computed and ATcT values in the case of the CH_3 + ICl product channel of the Cl + CH_3I reaction.[44]

Table 2 presents a comparison between the TST rate coefficients obtained in the present work and the ICVT/SCT rate coefficients reported by Jia and co-workers.[18] Significant deviations between the two sets of rate coefficients are observed, particularly at lower temperatures, whereas progressively better agreement is obtained with increasing temperature. The substantially larger rate coefficients obtained from the conventional TST treatment may partly originate from the simplified description of tunneling effects. At lower temperatures, where classical barrier crossing becomes increasingly unlikely because a smaller fraction of the reactants possesses sufficient energy to overcome the activation barrier, quantum-mechanical tunneling becomes progressively more important. In this regard, the SCT formalism employed within the ICVT/SCT framework provides a considerably more rigorous treatment of tunneling than the Wigner correction applied in the present TST calculations, which is based primarily on the imaginary frequency associated with the transition state. Furthermore, the presence of the low-energy entrance-channel minimum (IABS preMIN) may also contribute to the observed deviations. Following the initial encounter between the Cl atom and the C_2H_5I molecule, the system may spend a non-negligible amount of time within this entrance channel complex prior to product formation. Moreover, although the IABS preMIN is primarily associated with the iodine-abstraction pathway, structural reorganization within the loosely bound complex may still permit subsequent evolution toward the hydrogen-abstraction channel. Such dynamical effects are not fully accounted for within the conventional TST framework and may therefore contribute to the larger rate coefficients obtained in the present calculations. Finally, additional discrepancies may arise from the inherent limitations of the conventional TST formalism, which neglects recrossing effects. Within the TST approximation, every trajectory crossing the transition state is assumed to proceed directly toward products, whereas in reality a fraction of the trajectories may recross and return to the reactant region. By considering the entire minimum-energy path (MEP), the variational treatment employed within the ICVT/SCT framework partially accounts for such effects, thereby providing a more realistic kinetic description. Although our computations are performed at a higher level of electronic structure theory, thereby providing more reliable structural parameters, vibrational frequencies, and barrier heights – one of the dominant factors governing the rate coefficients within the TST framework – the computed barrier heights differ only moderately from the previously reported

Table 2 Comparison of our calculated and literature rate coefficients (10^{-13} cm^{-1} molecule^{-1} s^{-1}) for the Cl($^2P_{3/2}$) + C_2H_5I reaction at different temperatures. HABS TS1 and HABS TS2 denote the transition states identified in the present work, whereas TS1 and TS2 correspond to the literature transition states associated with the H-abstraction pathway from the CH_3 group. Similarly, HABS TS3 and TS3 refer to the present and literature transition states, respectively, for H abstraction from the CH_2 group of C_2H_5I

	Our work							Jia *et al.*[18]			
	HABS TS1		HABS TS2		HABS TS3		k_{sum}	TS1	TS2	TS3	k_{sum}
T/K	$k_{1,TST}$	$k_{1,TST+tunneling}$	$k_{2,TST}$	$k_{2,TST+tunneling}$	$k_{3,TST}$	$k_{3,TST+tunneling}$	$(k_1 + k_2)^a$	k_{TS1}	k_{TS2}	k_{TS3}	$(k_{TS1} + k_{TS2})^a$
220	2399.60	5067.63	3.08	8.87	3753.72	5676.78	5076.50	6.30	0.92	24.60	7.22
230	2026.11	4087.24	3.42	9.31	3031.34	4452.22	4096.54	6.71	1.11	26.60	7.82
250	1519.36	2827.57	4.16	10.22	2102.26	2936.30	2837.79	7.67	1.56	30.70	9.23
298	930.54	1494.43	6.24	12.64	1114.41	1425.58	1507.07	10.70	3.04	41.90	13.74
300	915.97	1463.66	6.33	12.74	1091.47	1392.19	1476.40	10.80	3.12	42.40	13.92
350	671.81	966.93	9.02	15.72	718.98	864.51	982.66	—	—	—	—
360	641.55	907.94	9.62	16.38	674.29	803.31	924.32	16.10	5.92	58.60	22.02
395	563.12	757.35	11.92	18.88	559.31	648.20	776.22	—	—	—	—
400	554.60	741.14	12.27	19.26	546.82	631.57	760.39	20.40	8.41	70.50	28.81
430	513.56	663.02	14.51	21.67	486.10	551.29	684.69	24.00	10.60	80.00	34.60
434	509.18	654.65	14.83	22.01	479.52	542.65	676.66	—	—	—	—
500	462.19	561.68	20.70	28.24	404.57	444.70	589.92	34.00	17.00	104.00	51.00
600	444.25	510.66	32.02	40.13	357.60	382.23	550.79	51.70	29.00	143.00	80.70
700	457.98	508.28	46.57	55.23	346.14	363.66	563.51	73.50	45.20	187.00	118.70
900	532.49	567.87	86.25	95.96	368.25	379.53	663.83	129.00	91.20	289.00	220.20
1000	584.54	616.00	111.68	121.86	391.35	401.06	737.86	162.00	121.00	346.00	283.00
1200	709.51	736.02	174.04	185.05	451.91	459.70	921.07	240.00	197.00	458.00	437.00
1400	857.10	880.63	251.77	263.48	526.45	533.11	1144.11	331.00	290.00	554.00	621.00
1500	938.22	960.66	296.33	308.34	567.89	574.15	1268.99	380.00	343.00	606.00	723.00

[a] Summed rate coefficient obtained from the rate coefficients calculated for the two transition states associated with the H-abstraction pathway from the CH_3 group.

values for the individual reaction pathways. Considering that the ICVT/SCT approach accounts not only for the transition-state region but also for the entire MEP, while additionally providing a more rigorous description of tunneling effects through the SCT formalism, the rate coefficients reported by Jia and co-workers[18] are likely to provide a more reliable kinetic description, particularly at lower temperatures.

IV. Summary and conclusions

The multichannel Cl($^2P_{3/2}$) + C_2H_5I reaction is investigated by comprehensively mapping the stationary-point geometries and corresponding energies with high-level *ab initio* methods, providing an accurate description of the underlying potential energy surface. Both abstraction and substitution pathways are investigated, including H- and I-abstraction channels and four substitution reactions proceeding *via* Walden inversion or front-side attack, involving single-atom (H, I) and group-substitution (CH_2I, CH_3) processes. The energy profile is constructed from CCSD(T)-F12b/aug-cc-pVDZ optimized geometries and CCSD(T)-F12b/aug-cc-pVQZ single-point energies, further corrected with scalar relativistic, core-correlation, spin–orbit, and post-CCSD(T) contributions to achieve higher accuracy. Thermodynamically, the I-substitution and H-abstraction channels are the most favorable, with the I-substitution representing the deeper one at −28.71(−27.98) kcal mol^{-1} relative to the reactants classically(adiabatically). Although the I-substitution pathway leads to more stable products, the H-abstraction process is kinetically preferred, exhibiting lower activation barriers regardless of the abstraction site on the C_2H_5I molecule. The lowest I-substitution barrier, corresponding to the Walden-inversion mechanism, appears at 13.59(13.13) kcal mol^{-1}, whereas even the highest H-abstraction barrier – associated with the abstraction of a H atom from the methyl group lying in the same molecular plane as the iodine substituent but positioned on the opposite side of the molecule – remains 8.23(12.51) kcal mol^{-1} lower in comparison. The H-abstraction can also proceed through two additional orientations. The abstraction occurring at the carbon bearing the iodine substituent features the lowest activation barrier not only among the H-abstraction channels but also across all examined reaction routes, with the corresponding transition state located 1.46(−2.65) kcal mol^{-1} above the reactants classically(adiabatically). The pathway in which the Cl atom abstracts a H from the methyl group situated on the side *trans* to the iodine atom requires slightly more energy, as the associated transition state lies at 2.03(−2.27) kcal mol^{-1}, placing its barrier between the other two H-abstraction pathways. The remaining reaction pathways – including iodine abstraction as well as CH_3-, CH_2I-, and H-substitution channels – are hindered both thermodynamically and kinetically, and therefore are less likely to contribute significantly to the observed product distribution. Notably, the overall reaction dynamics may also be influenced by the shallow minima identified in the entrance channel. One-dimensional potential energy scans performed for nine distinct orientations reveal two configurations exhibiting pronounced wells, one of which is successfully optimized to a stable pre-reaction complex with a classical(adiabatic) relative energy of −12.85(−12.27) kcal mol^{-1}. Finally, the most accurate structural parameters, vibrational frequencies, and benchmark adiabatic barrier heights obtained

in the present work are employed to estimate the rate coefficients associated with the hydrogen-abstraction pathway within the framework of transition-state theory. The new standard TST results are in disagreement with the previous ICVT/SCT rate coefficients,[18] which finding warrants future investigations.

Overall, the present study provides a comprehensive and high-accuracy characterization of the Cl + C_2H_5I potential energy landscape, revealing the thermodynamic and kinetic features governing the competing reaction pathways thereby supporting future kinetic modelling studies as well as potential energy surface developments that will facilitate a quantitative understanding of the reaction dynamics.

Conflicts of interest

There are no conflicts of interest to declare.

Data availability

The data that support the findings of this study are available from the corresponding author upon reasonable request.

Acknowledgements

We thank the National Research, Development and Innovation Office – NKFIH, K-146759 and the Momentum (Lendület) Program of the Hungarian Academy of Sciences for the financial support.

References

1 W. L. Chameides and D. D. Davis, *J. Geophys. Res.*, 1980, **85**, 7383.
2 R. J. Cicerone, *Rev. Geophys.*, 1981, **19**, 123.
3 Y. Yokouchi, H. Mukai, H. Yamamoto, A. Otsuki, C. Saitoh and Y. Nojiri, *J. Geophys. Res.*, 1997, **102**, 8805.
4 L. J. Carpenter, W. T. Sturges, S. A. Penkett and P. S. Liss, *J. Geophys. Res.*, 1999, **104**, 1679.
5 A. Sainz-Lopez, J. M. C. Plane, A. R. Baker, L. J. Carpenter, R. von Glasow, J. C. G. Martín, G. McFiggans and R. W. Saunders, *Chem. Rev.*, 2012, **112**, 1773.
6 L. Tinel, T. J. Adams, L. D. J. Hollis, A. J. M. Bridger, R. J. Chance, M. W. Ward, S. M. Ball and L. J. Carpenter, *Environ. Sci. Technol.*, 2020, **54**, 13228.
7 C. M. Roehl, J. B. Burkholder, G. K. Moortgat, A. R. Ravishankara and P. J. Crutzen, *J. Geophys. Res.*, 1997, **102**, 12819.
8 J. J. Orlando, C. A. Piety, J. M. Nicovich, M. L. McKee and P. H. Wine, *J. Phys. Chem. A*, 2005, **109**, 6659.
9 H. B. Singh and J. F. Kasting, *J. Atmos. Chem.*, 1988, **7**, 261.
10 R. Vogt, R. Sander, R. von Glasow and P. J. Crutzen, *J. Atmos. Chem.*, 1999, **32**, 375.
11 C. W. Spicer, E. G. Chapman, B. J. Finlayson-Pitts, R. A. Plastridge, J. M. Hubbe, J. D. Fast and C. M. Berkowitz, *Nature*, 1988, **394**, 353.
12 E. S. N. Cotter, N. J. Booth, C. E. Canosa-mas, D. J. Gray, D. E. Shallcross and R. P. Wayne, *Phys. Chem. Chem. Phys.*, 2001, **3**, 402.
13 E. S. N. Cotter, N. J. Booth, C. E. Canosa-Mas and R. P. Wayne, *Atmos. Environ.*, 2001, **35**, 2169.
14 V. Dookwah-Roberts, J. M. Nicovich and P. H. Wine, *J. Phys. Chem. A*, 2008, **112**, 9535.
15 S. Enami, S. Hashimoto, M. Kawasaki, Y. Nakano, T. Ishiwata, K. Tonokura and T. J. Wallington, *J. Phys. Chem. A*, 2005, **109**, 1587.
16 R. Wada, R. C. Scharma, M. A. Blitz and P. W. Seakins, *Phys. Chem. Chem. Phys.*, 2009, **11**, 10417.
17 R. Wada, K. Tonokura, S. Koba, T. Imamura, K. Nakai, H. Ushiyama, K. Matsumi, S. Enami and P. W. Seakins, *Chem. Phys. Lett.*, 2021, **762**, 138140.
18 X.-J. Jia, Y.-J. Liu, J.-Y. Sun, H. Sun, F. Wang, Z.-M. Su, X.-M. Pan and R.-S. Wang, *J. Comput. Chem.*, 2010, **31**, 2263.
19 H. Ihee, A. H. Zewail and W. A. Goddard, *J. Phys. Chem. A*, 1999, **103**, 6638.
20 O. Kong, J. Kim, M. Lorenc, T. K. Kim, H. Ihee and M. Wulff, *J. Phys. Chem. A*, 2005, **45**, 10451.
21 H. Ihee, M. Lorenz, T. K. Kim, Q. Y. Kong, M. Cammarata, J. H. Lee, S. Bratos and M. Wulff, *Science*, 2005, **309**, 1223.
22 J. Kim, J. H. Lee, J. Kim, S. Jun, K. H. Kim, T. W. Kim, M. Wulff and H. Ihee, *J. Phys. Chem. A*, 2011, **116**, 2713.
23 C. Møller and M. S. Plesset, *Phys. Rev.*, 1934, **46**, 618.
24 T. H. Dunning, *J. Chem. Phys.*, 1989, **90**, 1007.
25 T. B. Adler, G. Knizia and H.-J. Werner, *J. Chem. Phys.*, 2007, **127**, 221106.
26 T. H. Dunning Jr., *J. Chem. Phys.*, 1989, **90**, 1007.
27 K. A. Peterson, D. Figgen, E. Goll, H. Stoll and M. Dolg, *J. Chem. Phys.*, 2003, **119**, 11113.
28 K. A. Peterson, B. C. Shepler, D. Figgen and H. Stoll, *J. Phys. Chem. A*, 2006, **110**, 13877.
29 K. A. Peterson and T. H. Dunning, Jr., *J. Chem. Phys.*, 2002, **117**, 10548.
30 M. Douglas and N. M. Kroll, *Ann. Phys.*, 1974, **82**, 89.
31 W. A. de Jong, R. J. Harrison and D. A. Dixon, *J. Chem. Phys.*, 2001, **114**, 48.
32 D. H. Bross and K. A. Peterson, *Theor. Chem. Acc.*, 2014, **133**, 1434.
33 K. Raghavachari, G. W. Trucks, J. A. Pople and M. Head-Gordon, *Chem. Phys. Lett.*, 1989, **157**, 479.
34 J. Noga and R. J. Bartlett, *J. Chem. Phys.*, 1987, **86**, 7041.
35 M. Kállay and J. Gauss, *J. Chem. Phys.*, 2005, **123**, 214105.
36 K. R. Shamasundar, G. Knizia and H.-J. Werner, *J. Chem. Phys.*, 2011, **135**, 054101.
37 S. R. Langhoff and E. R. Davidson, *Int. J. Quantum Chem.*, 1974, **8**, 61.
38 A. Berning, M. Schweizer, H.-J. Werner, P. J. Knowles and P. Palmieri, *Mol. Phys.*, 2000, **98**, 1823.
39 National Institute of Standards and Technology (NIST), *NIST Atomic Spectra Database (ver. 5.12)*, https://physics.nist.gov/asd.
40 H.-J. Werner, P. J. Knowles, G. Knizia, F. R. Manby and M. Schütz, *et al.*, *Molpro, version 2015.1, a package of ab initio programs*, see https://www.molpro.net.

41 H.-J. Werner, P. J. Knowles, *et al.*, *MOLPRO, version 2023.2, a package of ab initio programs*, see https://www.molpro.net.
42 M. Kállay, P. R. Nagy, D. Mester, Z. Rolik, G. Samu, J. Csontos, J. Csóka, B. P. Szabó, L. Gyevi-Nagy, B. Hégely, *et al.*, *MRCC, a quantum chemical program suite*, see https://www.mrcc.hu.
43 B. Ruscic and D. H. Bross, *Active Thermochemical Tables (ATcT) values based on ver. 1.130 of the Thermochemical Network*, Argonne National Laboratory, 2019, available at https://ATcT.anl.gov.
44 D. R. Gál, D. Papp and G. Czakó, *Phys. Chem. Chem. Phys.*, 2024, **26**, 17695.